

# HyperGal: hyperspectral scene modeling for supernova typing with the Integral Field Spectrograph SEDmachine

J. Lezmy<sup>1</sup>, Y. Copin<sup>1</sup>, M. Rigault<sup>1</sup>, M. Smith<sup>1</sup>, J. D. Neill<sup>2</sup>

<sup>1</sup> Université de Lyon, Université Claude Bernard Lyon 1, CNRS/IN2P3, IP2I Lyon, F-69622, Villeurbanne, France  
e-mail: lezmy@ip2i.in2p3.fr

<sup>2</sup> Division of Physics, Mathematics, and Astronomy, California Institute of Technology, Pasadena, CA 91125, USA

Received September 23, 2022; accepted xxx xxx xxx

## ABSTRACT

**Context.** Recent developments in time domain astronomy, like the Zwicky Transient Facility, have made possible a daily scan of the entire visible sky, leading to the discovery of hundreds of new transients every night. Among these detections, 10 to 15 are supernovae (SNe), which have to be classified prior to cosmological use. The Spectral Energy Distribution machine (SEDm), a low resolution ( $\mathcal{R} \sim 100$ ) Integral Field Spectrograph, has been designed, built, and operated to spectroscopically observe and classify targets detected by the ZTF main camera.

**Aims.** As the current `PYSEDm` pipeline can only handle isolated point sources, it is limited by contamination when the transient is too close to its host galaxy core; this can lead to an incorrect typing and ultimately bias the cosmological analyses, and affect the SN sample homogeneity in terms of local environment properties. We present a new scene modeler to extract the transient spectrum from its structured background, aiming at improving the typing efficiency of the SEDm.

**Methods.** `HYPERGAL` is a fully chromatic scene modeler, which uses archival pre-transient photometric images of the SN environment to generate a hyperspectral model of the host galaxy; it is based on the `CIGALE` SED fitter used as a physically-motivated spectral interpolator. The galaxy model, complemented by a point source for the transient and a diffuse background component, is projected onto the SEDm spectro-spatial observation space and adjusted to observations; the SN spectrum is ultimately extracted from this multi-component model. The full procedure, from scene modeling to transient spectrum extraction and typing, is validated on 5000 simulated cubes built from actual SEDm observations of isolated host galaxies, covering a large variety of observing conditions and scene parameters.

**Results.** We introduce the contrast  $c$  as the transient-to-total flux ratio at SN location, integrated over the ZTF  $r$  band. From estimated contrast distribution of real SEDm observations, we show that `HYPERGAL` correctly classifies  $\sim 95\%$  of SNe Ia, and up to 99% for contrast  $c \geq 0.2$ , representing more than 90% of the observations. Compared to the standard point-source extraction method (without the hyperspectral galaxy modeling step), `HYPERGAL` correctly classifies 20% more SNe Ia between  $0.1 < c < 0.6$  (50% of the observation conditions), with less than 5% of SN Ia misidentifications. The false positive rate is less than 2% for  $c > 0.1$  ( $> 99\%$  of the observations), which represents half as much as the standard extraction method. Assuming a similar contrast distribution for core-collapse SNe, `HYPERGAL` classifies 14% additional SNe II and 11% additional SNe Ibc.

**Conclusions.** `HYPERGAL` proves to be extremely effective to extract and classify SNe in the presence of strong contamination by the host galaxy, providing a significant improvement with respect to the single point source extraction.

**Key words.** Instrumentation: spectrographs - Galaxies: general - Supernovae: general - Methods: data analysis - Techniques: spectroscopic - Surveys

## 1. Introduction

In the last two decades, time-domain astronomy has become increasingly efficient, thanks to the ability of the surveys to (near) daily scan the entire visible sky. We can cite the Catalina Real-Time Transient Survey (Drake et al. 2009), PanSTARRS-1 (Kaiser et al. 2002), ASAS-SN (Shappee et al. 2014) and ATLAS (Tonry et al. 2018). A more recent survey is the Zwicky Transient Facility (ZTF, Bellm et al. 2019; Graham et al. 2019), successor of the Palomar Transient Facility (Law et al. 2009), and using a 47 deg<sup>2</sup> camera. With such equipment, ZTF detects  $O(10^2)$  transients of interest every night, instrumental artifacts and previously known sources excluded, with a typical  $5\sigma$   $r$  band AB magnitude limit of 20.5. Among them, 10 to 15 are new objects that have just appeared and became bright enough to be detected. Once the photometric detection is triggered, ZTF relays the alert to the Spectral Energy Distribution machine (SEDm,

Blagorodnova et al. 2018), an Integral Field Spectrograph (IFS) designed and built to spectroscopically type transients brighter than  $\sim 19.5$  mag, and operating on the Palomar 60-inch telescope. The core of the SEDm is a Micro-Lenslet Array (MLA) covering  $28'' \times 28''$ , subdivided into  $52 \times 45$  hexagonal spaxels, combined to a multi-band ( $ugri$ ) field acquisition camera, used for positioning and guiding.

Currently, the automated pipeline routinely used for IFS data reduction and supernova (SN) spectrum extraction is `PYSEDm` (Rigault et al. 2019). Since this pipeline intrinsically assumes the target is an isolated point source, it cannot properly handle the situation where the transient is close to its host galaxy core.

As a matter of fact, since August 2018,  $\sim 30\%$  of the observed SN show some severe host contamination which significantly decreases the confidence level of the classification, and  $\sim 10\%$  are just unusable. This situation has various undesirable effects. From a mere statistical point of view, discarding

SNe with too strong a host contamination reduces the type Ia SN (SN Ia) sample by 10 to 20%, which weakens the strength of the Hubble diagram anchor at low redshift. Furthermore, the wrong classification of SNe Ia could induce a significant bias in the cosmological analysis (e.g. Jones et al. 2017).

Finally, a more subtle effect is related to the galactic environment bias, which would be caused by selecting out host-contaminated SNe (Rigault et al. 2013). In the past years, numerous studies have shown that the SN Ia standardized luminosity is tightly correlated with the environment properties. Rigault et al. (2015, 2020) showed that, after standardization for light curve shape and color, SNe Ia having a large local specific Star Formation Rate are fainter by  $0.16 \pm 0.03$  mag. Other tracers, like host galaxy stellar mass (Kelly et al. 2010; Sullivan et al. 2010; Childress et al. 2013; Betoule et al. 2014) or just host morphology (Pruzhinskaya et al. 2020), are finding the same correlation between SN Ia luminosity and their environment. Recently, Briday et al. (2022) have shown that all these tracers are compatible with two SN Ia populations differing in standardized magnitude by at least  $0.12 \pm 0.01$  mag.

Some developments have been made to improve the robustness of the point source extraction by estimating the faintest isomagnitude contour separating the galaxy and the SN (Kim et al. 2022); however, this is not yet optimal in most problematic situations, i.e. when the SN is faint or located near the host core: it only brings a marginal 1.7% improvement in classification accuracy from the standard PYSEDm analysis.

One could think of handling the host contamination by interpolating the galaxy area under the transient from the external parts in the FoV. Unfortunately, there are several reasons for not using such method, beyond the mere signal-to-noise issue. First, the seeing, which makes the SN spread over the galaxy structure: as much as the host light is contaminating the SN flux, the reverse is also true, and it is not clear how far from the SN position one could consider the galaxy flux to be free of the point source signal. Furthermore, the host spatial structure under the SN extent – linear, concave or convex – is not known *a priori*, specially in a strongly structured region such as the galaxy core, which would prevent a clean and robust interpolation. Finally, an interpolation would assume that the host spectral features are spatially uniform under the SN extent, which again is usually not the case, specially close to the galaxy core.

In order to improve the final SN Ia sample in numerous ways, we present in this paper **HYPERGAL**<sup>1</sup>, a scene modeler specifically designed to handle the strong host contamination case, through a detailed hyperspectral galaxy modeling, complemented by a smooth background component and a point-source transient. The algorithm concept is based on two ideas: first, public multi-band wide photometric surveys can provide reference information on the host galaxy before the transient event; second, the required host galaxy cube (two spatial dimensions and one spectral one) can be estimated from pure photometric observations using a dedicated SED fitter as a physically motivated spectral interpolator. The resulting hyperspectral host model can then be projected in the observable space of the SEDm, taking into account all observational effects: relative geometry between the photometric pixels (px) and the IFS spaxels (spx), spatial (Point Spread Function, PSF) and spectral (Line Spread Function, LSF) Impulse Response Functions (IRF) of the SEDm, Atmospheric Differential Refraction (ADR), sky background and additional diffused light.

Sec. 2 describes the **HYPERGAL** pipeline, and validation tests on realistic simulations are presented in Sec. 3, to estimate the accuracy of the SN extraction as well as the SN typing itself, since this is what the SEDm is designed for. We will also show the improvement with respect to an isolated source extractor such as **PYSEDm**. A discussion of some hypotheses and possible future improvements can be found in Sec. 4.

## 2. HYPERGAL pipeline

This section presents the different processing steps from the required input to the transient spectrum extraction (Fig. 1). SN ZTF20aamifit, at redshift of  $z = 0.045$  as measured from strong  $H\alpha$  line in the host spectrum, will systematically be used for illustration; it was observed with the SEDm in February 17, 2020, at airmass 1.7 in poor seeing conditions ( $2''.4$  FWHM). The SN is  $\sim 2''.8$  away from its host galaxy core, close enough not to be considered as isolated (see Fig. 3).

### 2.1. Inputs

Three main inputs are necessary to **HYPERGAL**: the SEDm cube to be analysed, the archival photometric thumbnails, and the redshift of the target.

The SEDm IFS  $(x, y, \lambda)$  cube of the scene is built from the 2D raw spectroscopic exposures with **PYSEDm** (Rigault et al. 2019, Sec. 2). It includes all the components – transient point source, spatially and spectrally structured host galaxy, night sky background and spatially smooth diffused light – to be handled by the scene modeler (Fig. 2).

The archival multi-band photometric images of the transient environment, acquired *before* the SN explosion, are obtained from the PanSTARRS-1 (PS1)  $3\pi$  Steradian survey (Chambers et al. 2016) in all *grizy* bands, and queried at the SN location through the Image Cutout Server<sup>2</sup>. PS1 is chosen for its sky coverage compatible with ZTF (north of declination  $-30$  deg). Figure 3 shows an RGB image for ZTF20aamifit host galaxy, through the PS1 *grz* bands.

An analysis of spatially structured scenes (harboring 3 or more well resolved objects in the SEDm FoV) provides a precise estimation of a scale ratio of SEDm and PS1 pixel sizes of  $2.230 \pm 0.003$ , which, for a PS1 px scale of  $0''.25$ , corresponds to an effective SEDm spaxel size of  $0''.558$ . Once measured, this SEDm scale is fixed in the pipeline. To save computation time for the SED fit and the spatial projection step, PS1 images are first spatially rebinned  $2 \times 2$ .

The third input is the host galaxy redshift, required by the SED-based interpolation of the photometric images. Around 50% of the targets observed by the SEDm have a host galaxy spectroscopic redshift known beforehand (Fremling et al. 2020); for the others, a redshift is *a priori* estimated from a preliminary transient spectrum extraction, using the transient spectral features and the possible presence of emission lines from the host galaxy. While it would be theoretically possible to assess the host redshift directly during the scene modeling, we did not try to implement this feature yet (see Sec 4). Furthermore, the consequence of an inaccurate input redshift has not been studied for this analysis.

<sup>1</sup> The code is available online at <https://github.com/JeremyLezmy/HyperGal>.

<sup>2</sup> <https://pslimages.stsci.edu/cgi-bin/ps1cutouts>

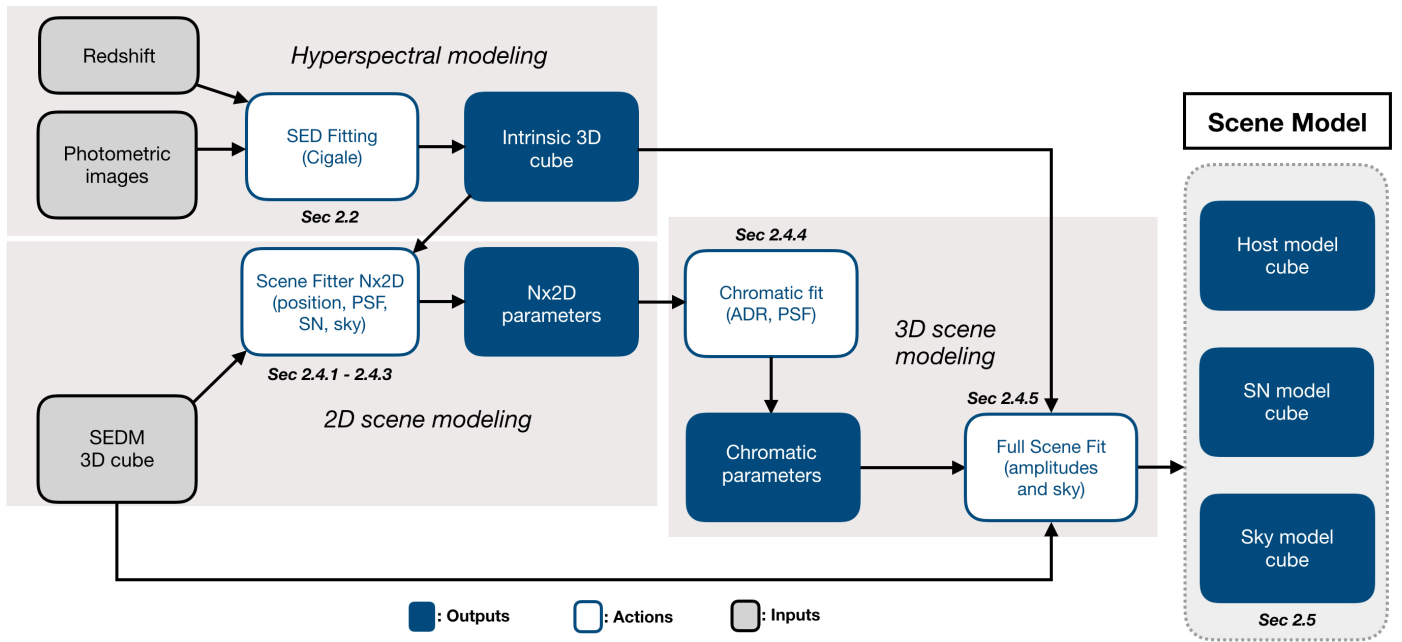


**Fig. 1.** Main processing steps of the **HYPERGAL** pipeline, and the sections where they are detailed.

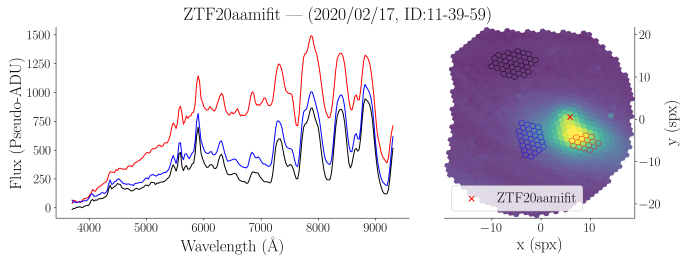


**Fig. 2.** SEDm cube from the observation of ZTF20aamifit. The *left panel* shows the spectra, whose color corresponds to the selected spaxels in the *right panel* (white image of the spectrally integrated cube). The *red cross* shows the SN position.

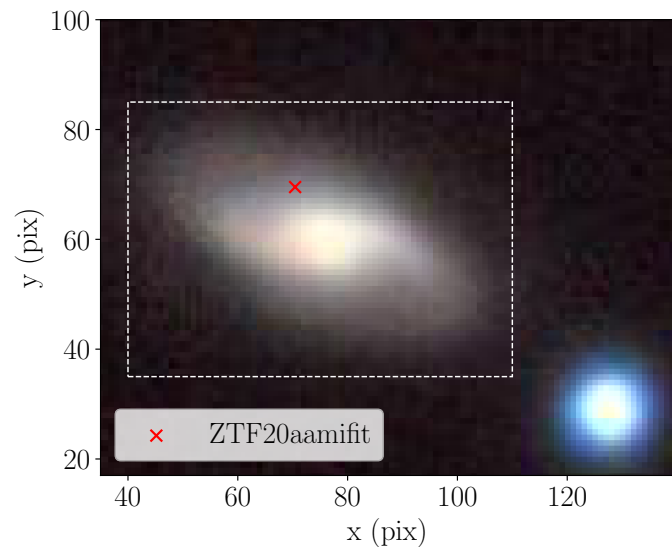


**Fig. 3.** RGB image of the host galaxy of SN ZTF20aamifit, constructed from the PS1 *grz* cutouts. The red cross shows the position of the SN detected by ZTF. The *x*- and *y*-axes are in native PS1 pixels, 0''25 aside. The white dashed box will be used as boundaries in Fig. 4 and 6.

## 2.2. SED fit

The SED fit aims to generate an effective hyperspectral – i.e. full 3D  $(x, y, \lambda)$  – host model from the *grizy* PS1 broadband images. During the process, each photometric pixel is treated independently, so that the resulting spaxel in the output cube gets its own spectrum. At the end of this process, this cube is still independent of the SEDm observation details (impulse responses, atmospheric effects, etc.). It is important to note that the SED fitter is not used here to derive accurate and spatially resolved physical parameters from the host galaxy, but rather to build a physically plausible spectral interpolation compatible with broadband archival images.

The software used for this step is **CIGALE**<sup>3</sup> (Burgarella et al. 2005; Noll et al. 2009; Boquien et al. 2019). It is based on a progressive computation, successively using modules describing a unique component of the SED. The set of all parameters tested by **CIGALE** is shown in Table 1.

### 2.2.1. Star Formation History and population

The time-evolution of the Star Formation Rate (SFR) is described by the Star Formation History (SFH) through the *sfhdelayed* module. Our SFH scenario includes two components, a delayed SFR and a late burst:

$$\text{SFR}(t) = \text{SFR}_{\text{delayed}}(t) + \text{SFR}_{\text{burst}}(t). \quad (1)$$

Both terms have a decreasing exponential form,

$$\text{SFR}_{\text{delayed}}(t) \propto \left( t / \tau_{\text{main}}^2 \right) e^{-t / \tau_{\text{main}}} \quad (2)$$

$$\text{SFR}_{\text{burst}}(t) \propto e^{-(t-t_0) / \tau_{\text{burst}}} \quad \text{for } t > t_0, \quad 0 \text{ otherwise.} \quad (3)$$

The amplitude of the late starburst is fixed by the parameter  $f_{\text{burst}}$ , defined as the ratio between the stellar mass formed during this event and the total stellar mass. The SFH is applied with the Initial Mass Function (IMF) from Chabrier (2003) on the stellar population model from Bruzual & Charlot (2003), used through the *bc03* module.

<sup>3</sup> Version 2020, <https://cigale.lam.fr>

## 2.2.2. Nebular emission

The light emitted in the Lyman continuum by the heaviest stars ionizes the gas in the galaxy. This physical process generates significant radiative emission in the continuum and spectral lines. This SED component is described by the nebular module, based on [Inoue \(2011\)](#). The model is effectively parameterized by the metallicity  $Z$  (the same as in the stellar population model `bc03`) and the ionization parameter  $\log(U)$ .

## 2.2.3. Dust extinction

Dust in the galaxy absorbs the radiation at short wavelengths, especially from the UV to the near-IR; this energy is then re-emitted in the mid- to far IR. As `HYPERGAL` is primarily targeting sources at redshift  $z < 0.1$  in the optical domain, extinction effect is properly considered through the dust attenuation module `dustatt_modified_CF00` from [Charlot & Fall \(2000\)](#). This approach is considering two star populations: the young ones ( $< 10^7$  years) still reside in their Birth Cloud (BC), and the old ones are considered as already dispersed in the InterStellar Medium (ISM). Attenuation is therefore treated differently: for the young population, both ISM and BC are considered, while for the old population, only the ISM is considered. In both case, the attenuation  $A_\lambda$  is modeled by a power law, normalized by the V-band attenuation:

$$A_\lambda^k = A_V^k \left( \frac{\lambda}{\lambda_V} \right)^{n_k} \quad k = \text{BC or ISM}, \quad (4)$$

with  $\lambda_V = 0.5 \mu\text{m}$ . The young-to-old star V-band attenuation ratio is parameterized through  $\mu = A_V^{\text{ISM}} / (A_V^{\text{ISM}} + A_V^{\text{BC}})$ , a free parameter allowing more flexibility and a better estimate of the H $\alpha$  emission lines ([Battisti et al. 2016](#); [Buat et al. 2018](#); [Malek et al. 2018](#); [Chevallard et al. 2019](#)). The power-law slope for the ISM is fixed at  $n_{\text{ISM}} = -0.7$  following [Charlot & Fall \(2000\)](#), and the slope for the BC at  $n_{\text{BC}} = -1.3$  as advocated in [da Cunha et al. \(2008\)](#).

For completeness, the `dale2014` module is used for the dust emission ([Dale et al. 2014](#)); however, this complex component has no significant impact in our spectral domain.

## 2.2.4. From SED fit to hyperspectral galaxy model

`CIGALE` is run using PS1 filter transmission curves from ([Tonry et al. 2012](#), see Fig. 6) on photometric pixels for which the Signal-to-Noise Ratio (SNR) is above 3 in all 5 bands. Otherwise, the output flux is set to 0 at all wavelengths: such pixels presumably belong to the sky or diffuse backgrounds, and cannot be properly modeled by the SED fitter.

For all fitted pixels, `CIGALE` returns a spectrum over an extended wavelength domain (from far UV to radio), with an inhomogeneous spectral sampling between 1 and 5 Å/px. All spectra are rebinned at the SEDm spectral sampling of  $\sim 26$  Å/px and truncated to the [3700, 9300] Å range, resulting in 220 monochromatic slices.

The broadband flux from the SED fit is compared to the input photometric measurements in Fig. 4, where is shown, for each PS1 band and pixel, the pull (i.e. the model residual normalized by the error on the data) and the relative RMS averaged over the 5 bands:

$$\text{RMS} = \sqrt{\frac{1}{5} \sum_{\lambda=\text{grizy}} \left( \frac{f_\lambda - \tilde{f}_\lambda}{f_\lambda} \right)^2} \quad (5)$$

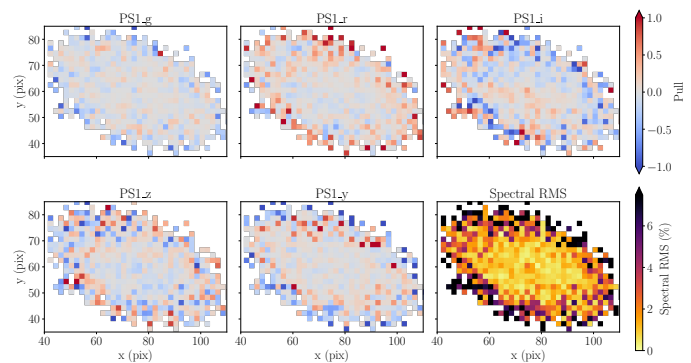


**Fig. 4.** From left to right and top to bottom: map of the pull for the *grizy* broadband images from `CIGALE` outputs, and spectral relative RMS over the 5 reference host images. Only pixels with SNR>3 for all *grizy* bands are considered (see Sec. 2.2).

where  $f_\lambda$  denotes the data and  $\tilde{f}_\lambda$  the predicted value. The averaged RMS is generally lower than 3% in the core of the galaxy, but can reach  $\sim 10\%$  in the outer parts. However, as the PS1 observations are 2 to 3 magnitude deeper than the SEDm ones ([Chambers et al. 2016](#)), relatively poorly fitted pixels far away from the host core have a marginal flux impact proportionately to the SEDm background, and do not significantly affect the transient spectrum in the scene model.

## 2.3. SEDm Impulse Response Functions

The “intrinsic” hyperspectral galaxy model obtained from the SED fit now has to be projected in the SEDm observation space, including the spectro-spatial IRFs. This section first presents the spectral component, i.e. the Line Spread Function (LSF), then the spatial component, aka the Point Spread Function (PSF).

### 2.3.1. Spectral IRF (LSF)

The output spectra from `CIGALE` have a spectral resolution of  $\sim 3$  Å in the wavelength range 3200 to 9500 Å (i.e. a median resolving power of  $\mathcal{R} = \lambda/\Delta\lambda \sim 2000$ , [Bruzual & Charlot 2003](#)), 20 $\times$  the near constant SEDm resolution ( $\mathcal{R} \sim 100$ , [Blagorodnova et al. 2018](#)). The full SEDm LSF is therefore a very good approximation of the differential spectral IRF between `CIGALE` and the SEDm.

To characterize the SEDm LSF, we use the intermediate line fits of the wavelength solution derived from arc-lamp observations, Cd, Hg, and Xe ([Rigault et al. 2019](#), Sec. 2.1.2). Each emission line is fitted by a single Gaussian profile over a 3rd-order polynomial continuum.

Studying wavelength calibration for 65 nights between 2018 and 2022, the LSF standard deviation  $\sigma_{LSF}$  turned out to be stationary (no evidence of evolution with time), fairly homogeneous in the FoV, but chromatic (as expected). Figure 5 shows the chromatic evolution of the standard deviation, and the quadratic polynomial model adjusted to it.

To adapt the `CIGALE` spectra to the SEDm resolution, the spectra of the hyperspectral galaxy model are convolved by the chromatic Gaussian LSF. An illustration of the result is shown in Fig. 6.



**Table 1.** Modules and input parameters used with `CIGALE`.

Parameters	Symbol	Tested values
<b>Star Formation History (SFH)</b>		
e-folding time of the main stellar population	$\tau_{\text{main}}$ (Gyr)	1, 3, 5
e-folding time of the late starburst population	$\tau_{\text{burst}}$ (Gyr)	10
age of the main stellar population	$\text{age}_{\text{main}}$ (Gyr)	1, 2, 4, 8, 10, 12
age of the late starburst	$\text{age}_{\text{burst}}$ (Myr)	10, 40, 70
mass fraction of the late starburst	$f_{\text{burst}}$	$0, 10^{-3}, 10^{-2}, 10^{-1}, 2 \times 10^{-1}$
<b>Stellar population</b>		
Metallicity	$Z$	$10^{-4}, 4 \times 10^{-4}, 4 \times 10^{-3}, 8 \times 10^{-3}, 2 \times 10^{-3}, 5 \times 10^{-2}$
<b>Nebular emission</b>		
Ionisation parameter	$\log(U)$	-4, -3, -2, -1
<b>Dust attenuation</b>		
InterStellar Medium attenuation in V	$A_V^{\text{ISM}}$	0, 0.3, 0.7, 1, 1.3, 1.7, 2
$A_V^{\text{ISM}}/(A_V^{\text{ISM}} + A_V^{\text{BC}})$	$\mu$	0.1, 0.3, 0.7, 1
BC power-law slope	$n_{\text{BC}}$	-1.3
ISM power-law slope	$n_{\text{ISM}}$	-0.7

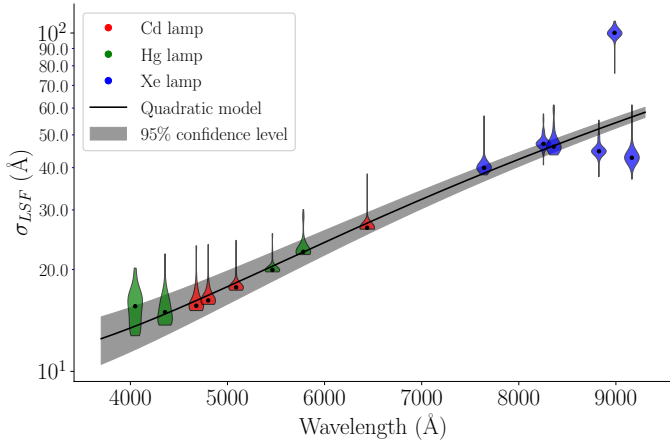


**Fig. 5.** LSF standard deviation  $\sigma_{\text{LSF}}$  as a function of wavelength, from the wavelength calibration of 65 nights between 2018 and 2022. Each violin corresponds to an emission line in the arc-lamp spectra (color legend).

### 2.3.2. Spatial IRF (PSF)

SNe are effective point sources, therefore solely described in the FoV by the SEDm PSF (and its amplitude). `HYPERGAL` uses a bisymmetric PSF model, in which radial profile is the sum of a Gaussian  $\mathcal{N}(r; \sigma)$  for the core, and a Moffat  $\mathcal{M}(r; \alpha, \beta)$  for the wings (Buton et al. 2013; Rubin et al. 2022):

$$\mathcal{P}(r; \alpha, \sigma, \beta, \eta) = \eta \times \mathcal{N}(r; \sigma) + \mathcal{M}(r; \alpha, \beta), \quad (6)$$

where  $r$  is an elliptical radius:

$$r^2 = (x - x_0)^2 + \mathcal{A}(y - y_0)^2 + 2\mathcal{B}(x - x_0) \times (y - y_0) \quad (7)$$

with  $(x_0, y_0)$  the coordinates of the point source. Parameters  $\mathcal{A}$  and  $\mathcal{B}$  simultaneously describe the flattening and the orientation of the PSF.

The 4 shape parameters  $(\alpha, \beta, \sigma, \eta)$ , which could be ill-constrained in low SNR regime if adjusted independently, are correlated by fixed relationships. The PSF was tested on 148 isolated standard stars, observed in 2021 with the SEDm, and we settled on the following model. The constrained PSF only has 2

free parameters:  $\alpha$  (Moffat radius) and  $\eta$  (relative normalization of the Gaussian), while the two other parameters are expressed as linear functions of  $\alpha$ :

$$\beta = \beta(\alpha) = \beta_0 + \beta_1 \alpha \quad (8)$$

$$\sigma = \sigma(\alpha) = \sigma_0 + \sigma_1 \alpha \quad (9)$$

where  $\beta_0 = 1.53$ ,  $\beta_1 = 0.22$ ,  $\sigma_0 = 0.42$  and  $\sigma_1 = 0.39$  were determined from the training star sample.

The chromaticity of  $\alpha(\lambda)$  is set as a power law function:

$$\alpha(\lambda) = \alpha_{\text{ref}} \left( \frac{\lambda}{\lambda_{\text{ref}}} \right)^\rho \quad (10)$$

where normalization  $\alpha_{\text{ref}}$  and index  $\rho$  are free parameters, and  $\lambda_{\text{ref}} \equiv 6000 \text{ \AA}$ . Parameters  $\eta$ ,  $\mathcal{A}$  and  $\mathcal{B}$  do not exhibit strong chromaticity, and are therefore considered constant.

Finally, the SEDm PSF of a given observation is fully described by 5 independent parameters:  $\alpha_{\text{ref}}$  and  $\rho$ ,  $\eta$ ,  $\mathcal{A}$  and  $\mathcal{B}$ .

### 2.3.3. Differential PSF between PS1 and SEDm

The original hyperspectral galaxy model is derived from PS1 photometric exposures, with different seeing conditions than the SEDm observations: the median seeing is  $\sim 1''.7$  in SEDm (Blagorodnova et al. 2018), and  $\sim 1''.2$  in PS1 images (Waters et al. 2020).

As the exact PSF profile is less critical for extended objects such as the host galaxy, we chose to model the differential PSF between PS1 and SEDm as a single bisymmetric Gaussian kernel, with free ellipticity and position angle. The hyperspectral model is thus convolved with this differential PSF before the spatial projection.

## 2.4. Scene modeling

The two main elements are now at hand to build the scene model:

- a hyperspectral host galaxy model, and the (differential) spectral and spatial IRF to match it to the SEDm observations,
- a chromatic PSF model for the transient point source.

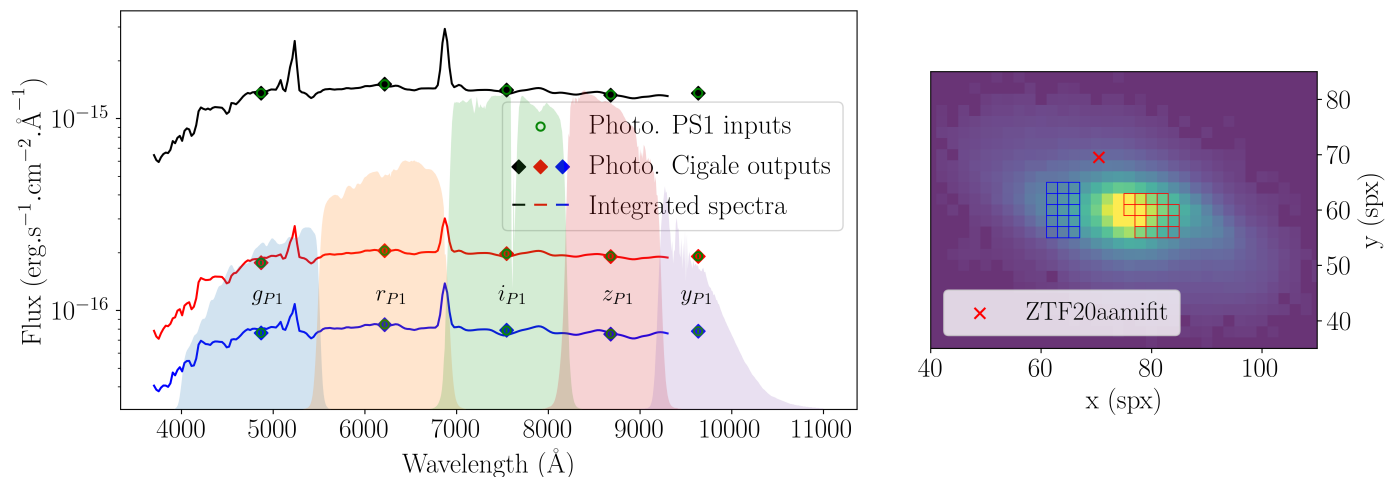


**Fig. 6.** Hyperspectral galaxy model of ZTF20aamifit host galaxy, after projection in the SEDm observation space (including LSF). The *green circles* correspond to the spatially integrated flux from PS1 cutouts, the *black diamonds* to the same quantities as fitted by CIGALE. The 5 shaded curves show the transmission of the *grizy* PS1 filters. The red and blue spectra on the left correspond to the spectra integrated in selected regions of same color in the model cube on the right; the black spectrum is the spectrum integrated over the full FoV.

The last component to complete the scene is the night sky and diffused light background, modeled with a 2D 2nd-order polynomial at each wavelength. The non-uniform terms handle a strong diffused light component, clearly visible in the edges of the SEDm FoV and spectral range. Overall, the background component is described by 6 parameters,  $b_0$ ,  $b_x$ ,  $b_y$ ,  $b_{xy}$ ,  $b_{xx}$  and  $b_{yy}$ .

We now describes the progressive method used to adjust it to the observed SEDm cube, and the detailed spatial projection procedure used to match the two cubes.

#### 2.4.1. General method

We first consider  $N \ll 220$  metaslices of the SEDm cubes, i.e. slices summed over a restricted wavelength domain, small enough to be considered roughly achromatic, but large enough to increase the SNR and significantly speed up the computation time. The scene is projected and fitted on all metaslices independently (the so-called “2D fit”, Sec. 2.4.3), which results in a set of  $N \times m$  parameters; some are nuisance parameters (e.g. background and component amplitudes), other key scene parameters, such as the point source position and PSF shape parameters.

From this set of parameters evaluated at  $N$  wavelengths, specific chromatic models are used to fix all shape and position quantities (the “1D fit”), for which the full spectral resolution is not required. Ultimately, HYPERGAL performs a final linear “3D” fit of the different component amplitudes over all monochromatic slices, providing the total scene model cube at original SEDm spectral sampling.

The pipeline uses by default  $N = 6$  metaslices linearly sampled between 5000 and 8500 Å. This spectral range is where the SEDm efficiency is higher than 70% (Blagorodnova et al. 2018), and is extended enough to well constrain the chromatic parameters, especially the ADR (see Sec. 2.4.4). The pipeline was tested with different number of metaslices, but no significant difference was noticed in the results.

HYPERGAL was extensively optimized with the parallel computing library DASK<sup>4</sup> (Dask Development Team 2016), a dynamic task scheduler working as well on single desktop machines as on many-node clusters. DASK optimizes the pipeline by

analyzing the (minimal) interdependencies between all computation tasks and building an optimal parallelized workflow to be submitted and run on an arbitrary number of available workers (in our case, we use 10 nodes on the IN2P3 Computing Center<sup>5</sup>).

#### 2.4.2. Spatial projection

The spatial projection of the hyperspectral galaxy model (matched to the SEDm spectral and spatial IRFs) is made by successively projecting each (meta)slice, taking into account the relative geometry and size between PS1-derived model (square, 0′50 aside) and SEDm (hexagonal, 0′558) spaxels. The projection is done according to a spatial anchor, a reference position in the sky supposedly known in both (meta)slice. The chosen anchor is the transient position, derived from the ZTF survey astrometry and located at the center of the queried PS1 images (and therefore at the center of the hyperspectral model). In the SEDm cube, this position is initially guessed from the astrometric solution of the SEDm Rainbow Camera (Blagorodnova et al. 2018; Rigault et al. 2019), but cannot be strictly fixed: the (chromatic) SEDm anchor position  $(x_0, y_0)$  is free in the fitting process of each metaslice.

The projection is made by geometrically overlapping the two polygonal spaxel grids, with the anchor position as a reference; this is effectively equivalent to a nearest neighbor interpolation scheme. These computations are done using SHAPELY<sup>6</sup> (Gillies et al. 2007–) and GEOPANDAS<sup>7</sup> (Jordahl 2014).

At this point, the model cube on which the PS1/SEDm differential PSF and the SEDm LSF are applied is now projected in the SEDm observation space, over the SEDm spaxel grid.

#### 2.4.3. Metaslice (2D) fit

As already mentioned, all components of the scene are first independently fitted on the  $N$  metaslices. The free parameters per metaslice are:

<sup>5</sup> <https://cc.in2p3.fr/>

<sup>6</sup> <https://github.com/Toblerity/Shapely>

<sup>7</sup> <https://github.com/geopandas/geopandas>

<sup>4</sup> <https://www.dask.org>

- the SN position  $(x_0, y_0)$  in the SEDm FoV, used as an anchor position for the spatial projection;
- the SN PSF parameters  $(\alpha, \eta, \mathcal{A}, \mathcal{B})$ ;
- the PS1/SEDm differential PSF parameters  $(\sigma_G, \mathcal{A}_G, \mathcal{B}_G)$ ;
- the amplitudes of the SN ( $I$ ) and host ( $G$ ) components;
- the background coefficients  $(b_0, b_x, b_y, b_{xy}, b_{xx}, b_{yy})$ .

We use `IMINUIT`<sup>8</sup> (James & Roos 1975; Dembinski et al. 2020) to minimize a weighted  $\chi^2$  for each metaslice independently:

$$\chi^2 = \sum_i \left( \frac{y_i - \tilde{y}_i}{\sigma_i} \right)^2, \quad (11)$$

where  $i$  runs on the spaxels of the metaslice,  $y$  and  $\tilde{y}$  are the data and model fluxes respectively, and  $\sigma$  the error on the data.

Fig. 7 illustrates the projection of one metaslice of the hyperspectral galaxy model onto the SEDm space. The fitted scene on this metaslice shows a spatial RMS between the model and the data of 2.6%. Although indicative of the overall scene model accuracy, a low RMS does not necessarily imply a clean separation of the different components, (e.g. when the transient lies on top of a sharp host galaxy core). Extraction accuracy is directly evaluated from simulated SN spectra in Sec. 3.

#### 2.4.4. Chromatic (1D) fit

Once the fit is performed independently over all  $N$  metaslices, a set of  $N$  chromatic estimates of the  $m$  parameters is at hand, and used to assess their (smooth) chromatic evolution (except for the component amplitudes and background parameters, which are nuisance parameters at this point).

The chromaticity of the full Gaussian + Moffat PSF is modeled as detailed in Sec. 2.3.2. The chromaticity of the width of the 2D Gaussian which models the differential PSF between PS1 and the SEDm is adjusted by a similar power law,

$$\sigma_G(\lambda) = \sigma_{\text{ref}} \left( \frac{\lambda}{\lambda_{\text{ref}}} \right)^{\rho_G} \quad (12)$$

where  $\rho_G$  and  $\sigma_{\text{ref}}$  are adjusted on the  $N$  metaslice estimates obtained previously, and  $\lambda_{\text{ref}} \equiv 6000 \text{ \AA}$ ; the shape parameters  $\mathcal{A}_G$  and  $\mathcal{B}_G$  are considered constant equal to their (inverse-variance weighted) mean values over the  $N$  metaslices.

The effective anchor location in the SEDm FoV is systematically wavelength-dependent, due to the chromatic light refraction through the atmosphere (ADR). Given the  $N$  positions of the SN in the different metaslices, an effective 4-parameter ADR can be fitted to track the chromatic offsets in the FoV:

$$\begin{bmatrix} x_0(\lambda) \\ y_0(\lambda) \end{bmatrix} = \begin{bmatrix} x_{\text{ref}} \\ y_{\text{ref}} \end{bmatrix} - \frac{1}{2} \left( \frac{1}{n^2(\lambda)} - \frac{1}{n^2(\lambda_{\text{ref}})} \right) \times \tan(d_z) \begin{bmatrix} \sin \theta \\ \cos \theta \end{bmatrix} \quad (13)$$

with  $(\theta, z, x_{\text{ref}}, y_{\text{ref}})$  the fitted parameters, where  $\theta$  is the parallactic angle,  $z$  the airmass and  $d_z = \arccos z^{-1}$  the zenith distance in the plane-parallel atmosphere approximation, and  $(x_{\text{ref}}, y_{\text{ref}})$  the reference position at reference wavelength  $\lambda_{\text{ref}} \equiv 6000 \text{ \AA}$ . The index of refraction  $n(\lambda)$  of air is computed using the Edlén equation from Stone & Zimmerman (2001)<sup>9</sup>, which takes into account the atmospheric pressure, temperature, and relative humidity, as provided for each exposure by the SEDm Telescope Control System.

Figure 8 illustrates the ADR effect, a drift of the metaslice anchor position with wavelength, and the ADR model, at effective airmass  $\sim 2.0$ .

<sup>8</sup> <https://github.com/scikit-hep/iminuit>

<sup>9</sup> <https://emtoolbox.nist.gov/Wavelength/Documentation.asp>

#### 2.4.5. Final (3D) fit

Once all PSF and ADR chromatic models are available from 2D+1D metaslice adjustments, the scene morphological parameters are considered known and fixed at each wavelength: the point source position  $(x_0, y_0)$  and PSF parameters  $(\alpha, \eta, \mathcal{A}, \mathcal{B})$ , as well as the PS1/SEDm differential PSF parameters  $(\sigma_G, \mathcal{A}_G, \mathcal{B}_G)$ . This allows us to perform a final 3D linear fit over all monochromatic slices, where only scaling amplitudes of the different scene components – namely host galaxy  $\{G\}$ , SN  $\{I\}$  and background polynomial components  $\{b_0, b_x, b_y, b_{xy}, b_{xx}, b_{yy}\}$  – are let free per slice. The total scene is then reconstructed at full spectral resolution.

Although  $G(\lambda)$  is primarily used to recover flux calibration mismatch between PS1 and SEDm, this normalization parameter can interfere in a non-trivial way with the position and intensity of the emission lines in the hyperspectral galaxy model. This effect might help to handle slightly incorrect input redshift used in the SED fitting step, especially under the assumption of a uniform spatial distribution of the line. As this has not been analysed in depth, we extend this thought in Sec. 4.

Fig. 9 presents the white image (spectral integral) of the final `HYPERGAL` scene model for SN ZTF20aamifit. The quality of the fit is evaluated from the pull map, showing no evidence of structured residuals. The spectral relative RMS map indicates an accuracy of  $\sim 4\%$  at SN and host core location, and 6 to 7% where only the background is significant.

### 2.5. Component extraction

The strength of the `HYPERGAL` pipeline is the simultaneous fit of the 3 scene components, the host galaxy, the transient point source and the background. The main quantity of interest is of course the SN spectrum (i.e. the vector of the point source amplitudes  $I(\lambda)$ , see Fig. 10), but one can also selectively subtract individual components to assess the quality of the scene model.

#### 2.5.1. Host galaxy integrated spectrum

Thus, the host contribution can be isolated in the SEDm cube by subtracting the SN and the background components (see Fig. 11). To further compute an integrated host spectrum, a large elliptical aperture is defined around the host with the `SEP` package (Barbary 2016; Bertin & Arnouts 1996) from the PS1 images. This aperture is then projected in the SEDm cube, using the respective World Coordinate Systems. Note that the ADR is neglected in the process, as it rarely induce a deviation of more than one or two spaxels in the FoV, and has barely any impact on the host spectrum integrated over a large aperture.

The integrated host spectrum is shown in Fig. 11, with the expected position of some major emission lines at the input redshift (independently of the host spectrum). This procedure highlights the consistency between the input redshift used for the hyperspectral galaxy modeling and the extracted integrated spectrum. In the future, it could be considered to consistently estimate the host redshift directly from such integrated spectrum during the scene modeling (see Sec. 4).

#### 2.5.2. Point source radial profile

Similarly, the point source contribution can be isolated in the SEDm cube by subtracting both host and background models, as shown in Fig. 12 for the  $[6167, 6755] \text{ \AA}$  metaslice of the ZTF20aamifit cube. This closer look at the point source contri-

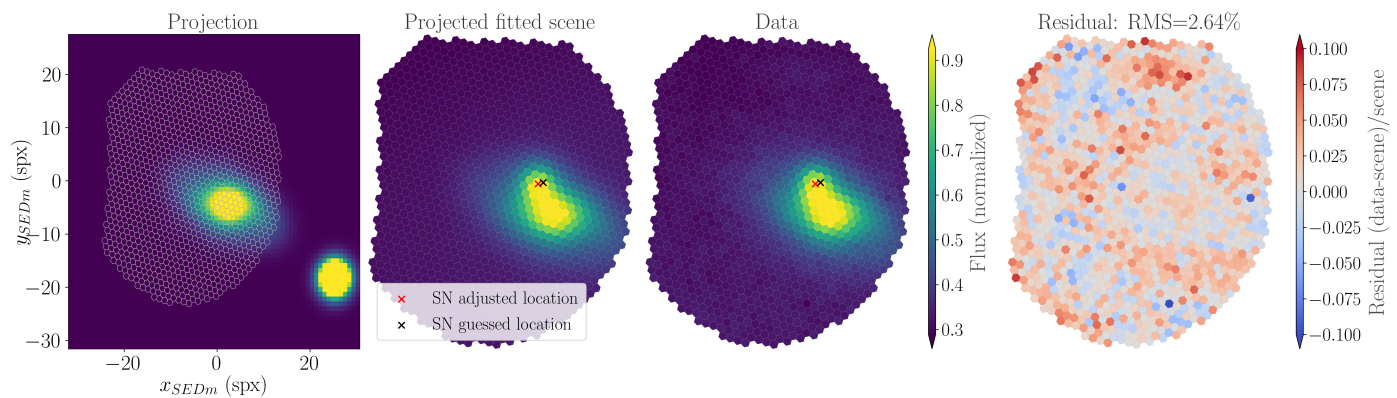


**Fig. 7.** Fit result for the [6167, 6755] Å metaslice of ZTF20aamifit cube. *From left to right:* metaslice from the original (transient-free) hyperspectral model with MLA footprint overlotted, projected fitted scene (host + background + SN), SEDm observations, and relative model residuals.

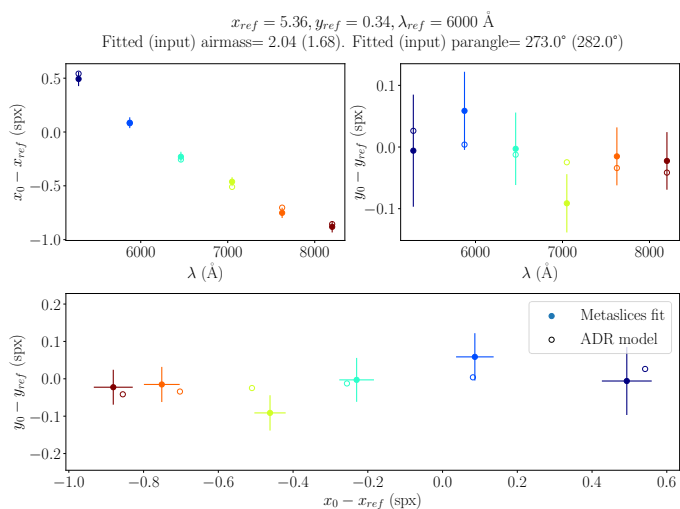


**Fig. 8.** SN positions as a function of wavelength, and the effective ADR fit. *Top panel:* relative offsets with respect to reference position at reference wavelength along each axis; filled points correspond to the observed offsets, and open circles to the predictions of the ADR model. *Bottom panel:* relative offsets in the  $(x, y)$  plane. Color codes for the central wavelength of the metaslices.

bution allows us to check the accuracy of the PSF profile in each metaslice. The fact that the profile smoothly tends to 0 means that the background was correctly modeled by `HYPERGAL`; also, the absence of outliers in the data points indicates that there is no evidence of residual host contamination in the profile, as noticed in the isolated SN image.

## 2.6. SN classification

`HYPERGAL` being primarily designed for the transient spectral classification, an automated typing procedure is included in the pipeline, based on the Supernova Identification (SNID [Blondin & Tonry 2007](#)). The typing is performed over the 4000 to 8000 Å spectral range, which includes the most discriminating spectral features for redshifts  $z \lesssim 0.1$ . This domain also corresponds to the one where the SEDm CCD quantum efficiency is over 60%.

The quality of the SNID classification is quantified by the  $rlap$  parameter, measuring the strength of the correlation between the input and template spectra. According to [Blondin & Tonry \(2007\)](#), an  $rlap \geq 5$  indicates a high confidence in the

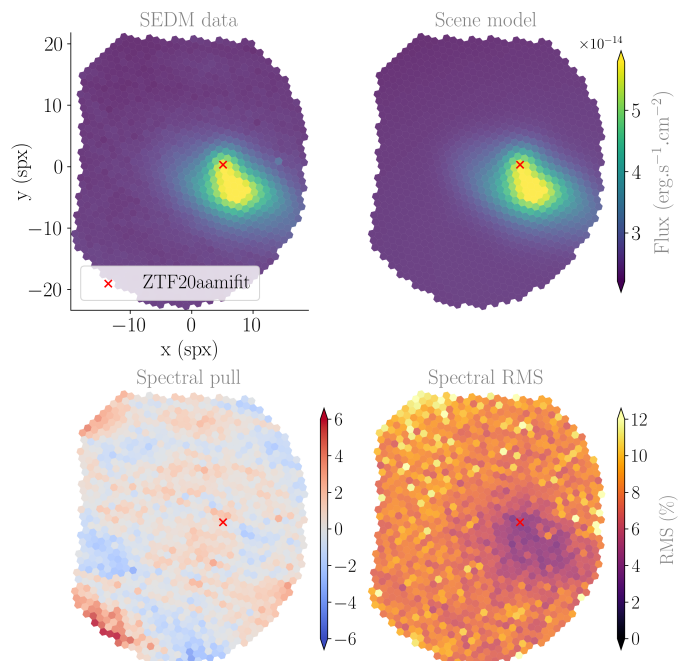


**Fig. 9.** Full scene model for ZTF20aamifit. *Top panel:* integrated SEDm and `HYPERGAL`-modeled cubes; the red cross indicates the adjusted point source position at 6000 Å. *Bottom panel:* spectral pull and spectral relative RMS. No galaxy- or SN-related structured residual is visible in the pull map and the spectral RMS indicates an accuracy of  $\sim 4\%$  at the host and SN locations.

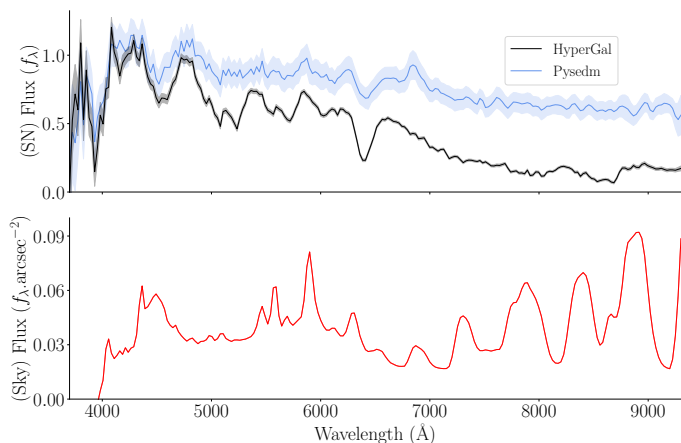
classification, without considering any prior on the redshift or the phase of the SN.

Figure 13 presents the SNID typing of ZTF20aamifit using its `HYPERGAL`-extracted spectrum. The best match has an  $rlap = 27$ , which leaves no doubt about its classification as an SN Ia. In comparison, the `PYSEDm`-extracted spectrum (see Fig. 10) is also typed as an SN Ia but with a significantly lower confidence ( $rlap = 9$ ).

## 3. HYPERGAL validation

The `HYPERGAL` pipeline is validated with a set of simulations, in order to quantify the accuracy of the extracted SN spectra as a function of various observational conditions, and the ability to spectrally classify the transient. In this section, we first present the simulation process, before performing some statistical anal-





**Fig. 10.** SN ZTF20aamifit spectrum – as extracted by **HYPERGAL** (black) and **PYSEDm** (blue) – and uniform sky spectrum (coefficient  $b_0(\lambda)$ , red). Flux unit  $f_\lambda$  stands for femto-erg  $\text{cm}^{-2} \text{s}^{-1} \text{\AA}^{-1}$ .

ysis on the spectral accuracy, followed by the typing efficiency. For comparison, the SNe are also extracted with a method similar to **PYSEDm** (Rigault et al. 2019), that is a plain PSF extraction of a supposedly isolated source (not accounting for the background galaxy), but using the same PSF and diffuse background models as **HYPERGAL** for consistency.

### 3.1. Simulated sample

During a short shutdown of the main ZTF camera, the SEDm was free to observe a few galaxies which hosted SNe at least one year earlier. These observed host cubes are therefore naturally in the SEDm space for which **HYPERGAL** is designed; 10 different hosts with various morphologies were acquired at different locations in the IFU and with an airmass ranging from 1.01 to 2.04. This allows us to cover a large variety of observation conditions, from the ideal case to the poorest condition. An artificial point source, whose spectrum and type is known a priori, is then added to these cubes.

To mimic SEDm spectra as much as possible, we use spectra of well-isolated transients observed with SEDm and successfully classified by SNID with a very high  $rlap$ . For the SNe Ia (the most numerous to be observed), 70 spectra are selected with  $rlap > 25$  for the best model and  $rlap > 15$  for the first 30 models. Similarly, 7 SNe II spectra with  $rlap > 12$  are selected. For the more rarely observed SNe Ic and SNe Ib ( $\sim 5\%$  of observations), only one spectrum of each was chosen, but with high classification confidence ( $rlap \sim 22$  for the Ib and  $rlap \sim 13$  for the Ic). To increase the SNR, each of these spectra is then slightly smoothed using a Savitzky-Golay filter (3rd-order polynomial over a window of 5 pixels), in order to keep intact the spectral structures.

While building the simulated sample, the different SN types are distributed to follow the observed fractions (Fremming et al. 2020), with 80% of SNe Ia, 15% of SNe II, 2.5% of SNe Ib, and 2.5% of SNe Ic. For further analysis, Ib and Ic will be studied jointly as SNe Ibc.

A marginalization on the phase of the SNe Ia is applied, based on the DR1 statistics from the ZTF SN Ia group (Dhawan et al. 2022). Knowing the phase of the 70 SN Ia input spectra used for the simulation, we draw the SN templates to follow the observed distribution of phases, modeled as a Gaussian distribution centered on  $-3$  days with a standard deviation of 4 days.

Concerning the PSF, the profile is assumed to follow the model presented in the Sec. 2.3.2. To faithfully represent the seeing diversity of the observations, the chromatic radial profile parameters are drawn from the joint distribution built from  $\sim 2000$  standard stars, thus taking into account the latent correlations between parameters.

Finally, 2 extra parameters – which we consider the most likely to impact on the **HYPERGAL** robustness – are introduced in the simulations: the contrast  $c$  between the transient and the local background, and the distance  $d$  between the target and the host.

The latter aims to cover all observed cases, from the exact overlapping between the point source and the host ( $d \approx 0$ ) to the limit of an unstructured background ( $d \gg$  host core size). The host center is identified by matching the WCS solution from the SEDm cube and the underlying photometric images from PS1. The distance  $d$  is drawn from a uniform distribution between 0 and  $5''6 \equiv 10$  spx. As the SEDm mostly observes well centered point sources, the simulated SN is placed within 12 spx from the center of the FoV, or at least towards the MLA center if the host is on the edge.

The contrast  $c$  is defined by  $c = S/(S + B) \in [0, 1]$  where  $S$  is the transient signal, and  $B$  is the total (sky and host) background, both spectrally integrated over the equivalent  $r$  band of ZTF. For a random  $c$  drawn from a uniform distribution in  $[0, 1]$ , the background signal  $B$  is first estimated at the simulated SN location, by successively integrating spatially the pure host cube weighted by the chromatic PSF profile, then spectrally over the ZTF  $r$  band. Once  $B$  is known, the SN spectrum is scaled so that the  $r$ -band integral  $S = cB/(1 - c)$ . Finally, the simulated SN contribution to the cube variance is added to the one from the host galaxy, under the hypothesis of pure photon noise, using the flux solution of the host cube.

Ultimately, the 5000 simulated cubes are built, covering a large range of observation conditions, host galaxy morphologies and positions in the FoV, transient locations and spectral types and SNR. The **HYPERGAL** pipeline and the standard point source extraction are then used to estimate the resulting SN spectra.

### 3.2. Extraction accuracy

The SEDm is designed and used for the spectral classification of transient. Thus, beyond pure absolute spectro-photometric flux accuracy, what is important is the capacity of **HYPERGAL** to extract the spectral features allowing a proper classification, independently of the absolute flux level or even the large-scale continuum shape. Consequently, the **HYPERGAL** performances are evaluated on continuum-normalized transient spectra in the  $[4000, 8000] \text{\AA}$  wavelength range, as in SNID.

The continuum is fitted as a 5th-order polynomial over the wavelength range slightly extended by  $100 \text{\AA}$  at each extreme, to avoid some unwanted boundary effects. The spectral comparison between simulation input and **HYPERGAL**/standard method output spectra is then systematically performed on continuum-normalized spectra, and is quantified using a wavelength-averaged relative RMS similar to Eq. (5):

$$\text{RMS} = \sqrt{\frac{1}{N} \sum_{\lambda} \left( \frac{f_{\lambda} - \tilde{f}_{\lambda}}{f_{\lambda}} \right)^2} \quad (14)$$

where  $N$  refers to the number of monochromatic slices between  $[4000, 8000] \text{\AA}$ ,  $f_{\lambda}$  denotes the data and  $\tilde{f}_{\lambda}$  the predicted value.

The distance  $d$  is found to have no influence on the spectral accuracy of **HYPERGAL**, with an absolute correlation coefficient

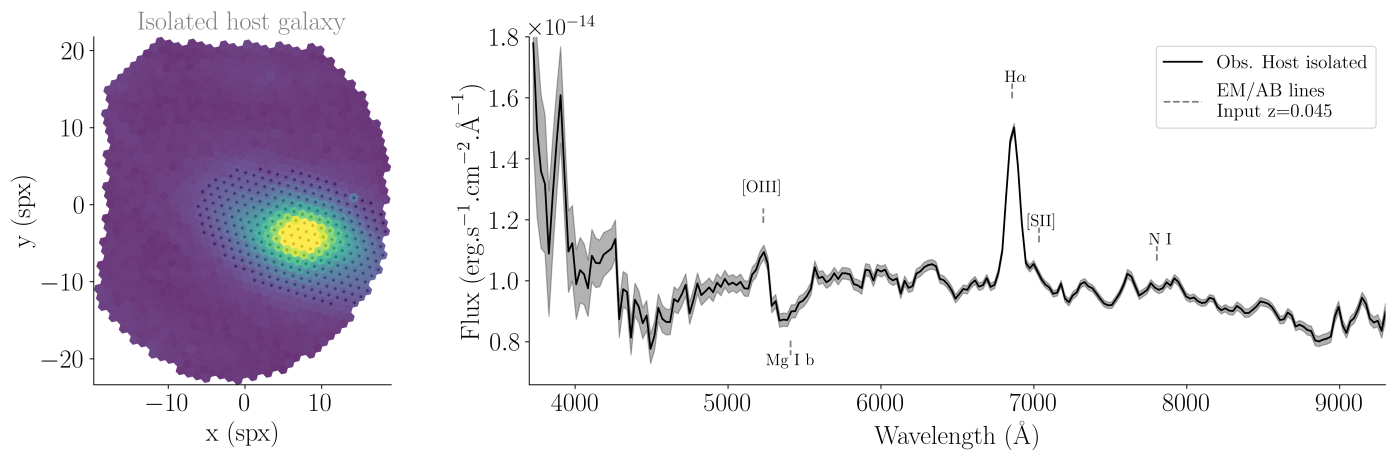


**Fig. 11.** ZTF20aamifit host galaxy, isolated from the SEDm data cube. *Left panel:* isolated host galaxy component in the SEDm cube, after subtraction of both the SN and background models. *Right panel:* host spectrum integrated over the selected spaxels; the main spectral features are marked for the input redshift  $z = 0.045$ .

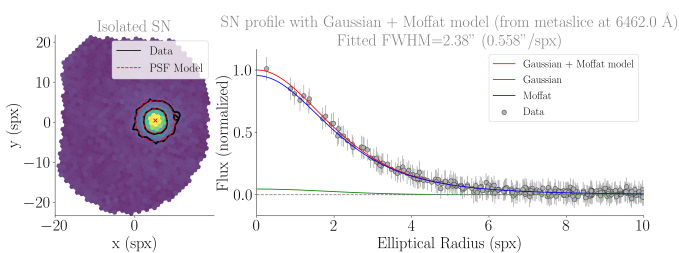


**Fig. 12.** SN ZTF20aamifit, isolated from the SEDm data cube. *Left panel:* isolated SN component in the SEDm [6167, 6755] Å metaslice, after subtraction of both the host and background models; the *red cross* indicates the fitted SN location, and *contours* show the elliptical isoradius at 3 and 5 spax for observations (*black solid lines*) and model (*red dashed lines*). *Right panel:* PSF profile for the same metaslice, as a function of the elliptical radius. The data points refer to the isolated SN on the left panel, the *red curve* corresponds to the PSF profile (without the background), the *blue* and *green curves* to the Moffat and the Gaussian components respectively. The Gaussian component is particularly weak because of the poor seeing conditions.

lower than 0.2. On the other hand, Fig. 14 shows the correlation between spectral relative RMS and contrast  $c$  for both extraction methods on continuum-normalized spectra. The results are marginalized over all SN types, as the extraction accuracy is supposed independent of the spectral shape.

Both methods obtain an RMS greater than 20% for  $c < 0.2$ , suggesting that spectral classification at such low contrast will be difficult. Yet, the standard method seems to be more accurate than **HYPERGAL** at extremely low contrast ( $c < 0.1$ ); this actually appear to be an artifact of the continuum normalization. At very low contrast, neither methods can reasonably disentangle the SN from the background; however, by effectively mixing SN and host signal, the standard point source extracted spectrum has a higher SNR (although less accurate), and the continuum normalization is less prone to fail catastrophically, contrary to the case of the spectrum consistent with 0 as extracted by **HYPERGAL**.

**HYPERGAL** starts to stand out for  $0.2 < c < 0.3$  with a median RMS around 10%, and RMS decreases steadily below 10% at  $c > 0.3$ , 5% for  $c > 0.5$ , and 1% for  $c > 0.8$ . Compared to the standard extraction method, **HYPERGAL** shows a median improvement of  $\sim 50\%$  for  $0.2 < c < 0.6$ , and gradually returns to a median improvement of  $\sim 20\%$  up to highest contrasts. Since the

continuum normalization removes the effects of absolute scaling and color terms on the spectral RMS, the improvement exclusively relates to the contamination of the SN spectrum by the host galaxy spectral features. This demonstrates the effectiveness of **HYPERGAL** to drastically reduce this host contamination.

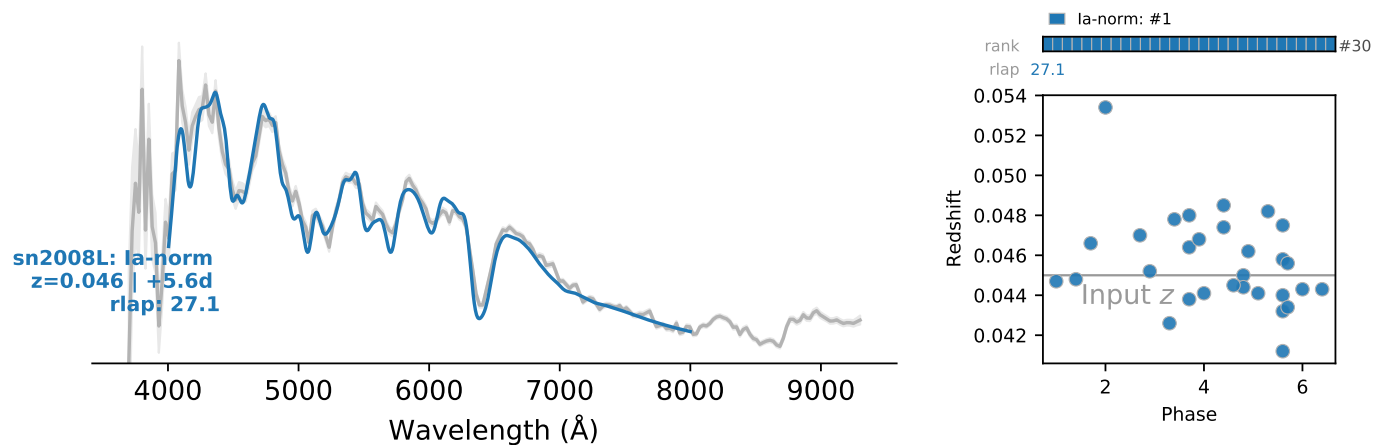
### 3.3. Distribution of contrast in the observations

Before turning to the classification efficiency, the contrast distribution in the SEDm observations is estimated, as a reference to compare our results with. Rather than using **HYPERGAL** on observations made with the SEDm (as was actually done for the ZTF Cosmology SN Ia Data Release 2 to come [Rigault et al. in prep](#)) – this would be like evaluating the pipeline with itself – the contrast  $c = S/(S + B)$  is estimated from photometric images of the same DR2 sample, made up of about 3000 SNe Ia.

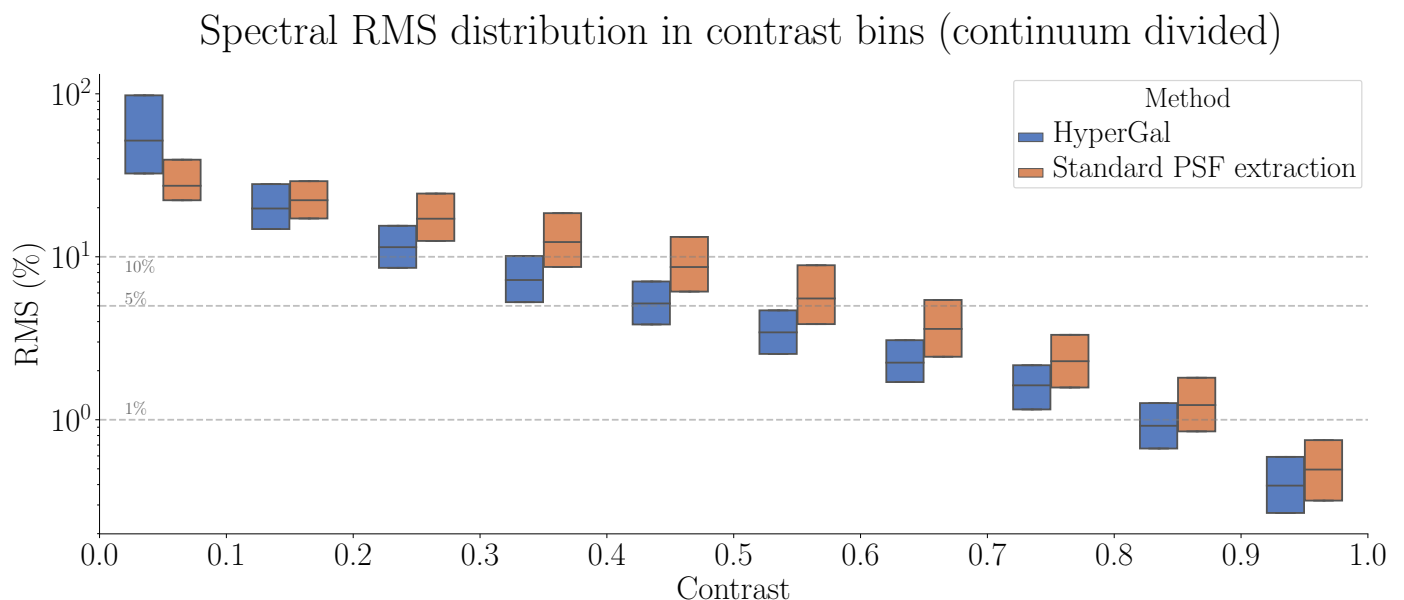
For each SN, its signal  $S$  in the PS1  $r$  band at the date of the SEDm observation is estimated from the SALT2 fit ([Guy et al. 2005, 2007](#); [Betoule et al. 2014](#)) of its light curve. We chose the PS1  $r$  band, in practice very similar to the ZTF one, because only images from this survey were available at the time of the study. On the other hand, the host contribution to the background  $B_{gal}$  is estimated from the integrated flux within a radius of  $2''$  around the SN. As PS1 images are already sky-subtracted, an additional sky background  $B_{sky}$  has to be added for a fair comparison with simulations. Two different values are used: a fiducial value  $m_{sky} = 20$  mag, approximately corresponding to the magnitude depth of the SEDm, and a more conservative value  $m_{sky} = 21$  mag. The sky background being largely negligible in front of a galactic one, its exact value essentially alters the high contrast values: for a SN isolated from its host galaxy, the contrast would systematically increases as the sky background tends to 0.

Figure 15 displays the cumulative distribution of the contrast for the DR2. The median contrast of this distribution is  $c = 0.58$  for  $m_{sky} = 20$  mag and  $c = 0.63$  for  $m_{sky} = 21$  mag. For both sky levels, less than 1% of observations have a contrast  $c < 0.1$ , and only 7% with  $c < 0.2$ . At high contrast end, 2 to 5% of the observations have a  $c > 0.9$  depending on the adopted sky magnitude. Almost 95% of observations have a contrast  $0.1 \leq c \leq 0.9$ , and a slightly less than 90% with  $0.2 \leq c \leq 0.9$ .

According to the results of Sec. 3.2, one can therefore assess the spectral accuracy of **HYPERGAL** on the DR2 sample – using



**Fig. 13.** SNID typing of the ZTF20aamifit HYPERGAL spectrum. *Left panel:* input spectrum (in grey) and best model from SNID (in blue). *Right panel:* distribution in the (redshift, phase) plane of the 30 best matches with an  $rlap > 5$  (all being normal SNe Ia in this case). The input redshift of the galaxy ( $z = 0.045$ ) is indicated with the horizontal grey line. The best model, with a very high  $rlap = 27$ , classifies ZTF20aamifit as an SN Ia at redshift  $z = 0.046$  and phase  $p = +5.6$  days.



**Fig. 14.** Distribution, as a function of the contrast, of the spectral relative RMS between simulation input spectra and extracted spectra, averaged over the  $[4000, 8000]$  Å domain. In the boxes, the 3 levels represent the 3 quartiles (25%, median, and 75%). Each bin includes the same number of simulations, as the contrast  $c$  is uniformly distributed in  $[0, 1]$ .

the spectral relative RMS (Eq. 14) as an indicator – to be of the order of 10%, 5% and 2% for 80%, 60% and 20% of the observations respectively. In comparison, the standard extraction method reaches these levels for 60%, 45% and 15% of the observations.

### 3.4. Typing efficiency

As mentioned earlier, the most important validation result in the context of the SEDm is the efficiency of HYPERGAL to spectrally classify the target SN. The test on the simulated cubes is performed using the same classifier as in ZTF, i.e. SNID; the confidence criteria given for the classification are however slightly stricter, as we regularly identified false positives (i.e. SN erroneously classified as Ia) in the current PYSEDm pipeline. The minimum  $rlap$  is set to  $rlap_{\min} = 6$  (rather than 5) for the best-fit model; furthermore, at least 50% of the top-10 models have to

be of the same type as the best one to confirm a classification. If one of these criteria is not met, the spectrum is classified as “uncertain”.

Figure 16 shows the typing efficiency from HYPERGAL, and the improvement with respect to the standard extraction method without host modeling. Contrary to the previous RMS analysis, results are presented for each SN type, since the spectral signatures are different in all SN types.

As anticipated in Sec. 3.2, both methods are definitely not reliable for contrasts below 0.1. SNe Ia are more easily classified, due to the quantity and strength of features in their spectra: the typing success is 71% for SNe Ia for  $0.1 \leq c \leq 0.2$  ( $\sim 7\%$  of real observations); types Ibc and II on the other hand are correctly classified with a success rate of 23% and 35% respectively.

For  $0.2 < c < 0.3$ , the typing success reaches more than 96% for SNe Ia, 77% for Ibc and 51% for SNe II. More than 99%

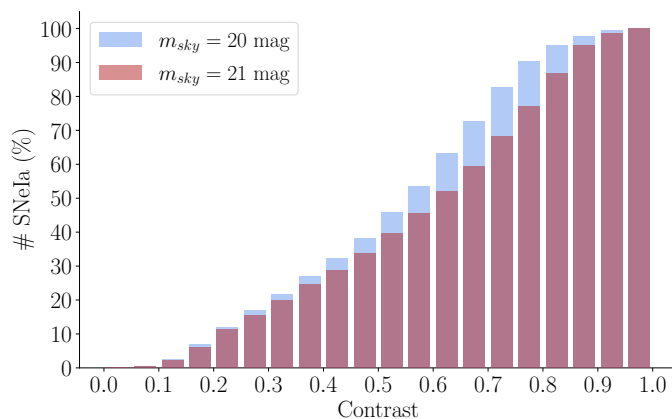


**Fig. 15.** Cumulative contrast distribution estimated from  $\sim 3000$  SN Ia observed with the SEDm. Since only  $B_{gal}$  is estimated from PS1 images, an additional  $B_{sky}$  is estimated using two different sky levels,  $m_{sky} = 20$  (blue) for a realistic value, and  $m_{sky} = 21$  (red) for a conservative value.

of SNe Ia are correctly classified with  $c > 0.3$ , and more than 95% of all SNe for  $c > 0.4$ . With  $\sim 84\%$  of observations having a contrast  $c > 0.3$ ,  $\sim 9\%$  with  $0.2 < c < 0.3$  and  $\sim 7\%$  with  $0.1 < c < 0.2$ , one can conclude that **HYPERGAL** can successfully classify nearly 95% of all SNe Ia observed by SEDm. For a contrast  $c \geq 0.2$  (which represents more than 90% of the real observations), nearly 99% of SNe Ia are properly classified. The improvement brought by **HYPERGAL** over the standard extraction method is obvious, with a sweet spot in  $0.1 < c < 0.6$ : this will result in more than 30% of additional SNe correctly classified.

The main spectral feature of SNe II being the  $H\alpha$  emission line, usually highly contaminated by the host galaxy, **HYPERGAL** allows a significant improvement for this particular type, from 15% to 37% of additional correctly classified SNe II in the  $0.1 < c < 0.6$  range; for SNe Ibc, the difference only appears from  $c > 0.2$ , with similar gains between 13% and 31%. SNe Ia having a lot of strong and easily identified spectral features, the boost from the standard method is slightly less manifest, but stays highly significant, from 30% of additional correctly classified SNe Ia for  $0.1 < c < 0.2$  to 5% when  $0.5 < c < 0.6$ . For  $c > 0.6$ , when the SN ostensibly stands out of the galaxy, the difference between the two methods becomes marginal whatever the SN type.

Taking into account the contrast distribution of the observations, **HYPERGAL** should significantly improve the classification of SNe Ia in nearly 50% of the observations (the other half being also properly classified by the standard extraction method). As 50% of the observations have  $0.1 < c < 0.6$ , **HYPERGAL** will allow the correct classification of almost 20% more SNe Ia in this interval, corresponding to 10% of all SNe Ia classifiable with the SEDm. Assuming a similar contrast distribution for all SN types, **HYPERGAL** will classify 14% additional SNe II and 11% SNe Ibc.

To probe the critical contamination of the SN Ia sample by core-collapse SNe, the False Positive Rate (FPR) for SN Ia is examined. Figure 17 shows that **HYPERGAL** has a significantly lower FPR than for the standard method. Excluding the unrealistically low contrast cases ( $c < 0.1$ ), **HYPERGAL** shows a progressive decrease in FPR from 8% to 1% for contrast rising from 0.1 to 0.6 (FPR is null beyond that); in comparison, the standard method oscillates between 6 and 9% in same contrast range. As a conclusion, the **HYPERGAL** FPR is on average less than 5% for contrasts between 0.1 and 0.6 ( $\sim 50\%$  of the observations), and

less than 2% for  $c > 0.1$  (more than 99% of all observations); this is half as much as the standard extraction method.

## 4. Discussion

We now discuss some limitations of the current **HYPERGAL** implementation, and possible future developments.

Regarding the validation methodology, we acknowledge some simplifications with respect to actual observations. For instance, the true distance distribution between the SN and its host was not explicitly modeled, i.e. this parameter was marginalized uniformly between 0 and 5''6. As a full-scene modeler which properly handles this parameter and therefore shows little sensitivity to it (Sec. 3.2), this approximation does not impact the **HYPERGAL** results; this is not true for the single point-source method which critically depends on the transient-host distance. Overall, we think the validation approximations actually tend to minimize the improvement of **HYPERGAL** with respect to the standard method.

Undoubtedly, the most limiting constraint from **HYPERGAL** is the need for an external redshift measurement of the host galaxy, an a priori needed by the SED fitter used as a physically-motivated host galaxy spectral interpolator, and of critical importance for the treatment of emission lines. In practice, this is not so much of an issue: in the current ZTF sample, about 50% of SN hosts already have a spectral redshift, mostly from SDSS surveys (Fremling et al. 2020), with a precision of  $\sigma_z \sim 10^{-5}$  for  $z < 0.1$  (Bolton et al. 2012); the remaining 50% of SNe have a redshift deduced from a preliminary extraction of the SN spectrum, either from low-resolution spectral features in the SN spectrum ( $\sim 40\%$ ) or emission lines of the host galaxy having contaminated the SN spectrum ( $\sim 10\%$ ). In both cases, the redshift is estimated by SNID with a precision of  $\sigma_z \sim 5 \times 10^{-3}$  (Fremling et al. 2020). Furthermore, 95% of ZTF SN hosts are brighter than 20 mag, allowing other surveys such as the Dark Energy Spectroscopic Instrument (DESI) Bright Galaxy Survey (DESI Collaboration et al. 2016) to systematically provide a large fraction of spectral redshifts in the future.

A slightly incorrect input redshift (encoded as a wavelength offset of the emission line position in the hyperspectral galaxy model), as well as an approximate SED fit of the emission line fluxes (marginally constrained by broadband photometric observations) is corrected to first order by the monochromatic galaxy amplitudes  $G(\lambda)$  during the ultimate 3D fit. Primarily introduced to recover flux calibration mismatch between PS1 and SEDm, this normalization parameter actually interferes in a non-trivial way with the position and intensity of emission lines in the brightest parts of the scene to minimize residuals between fixed (at this stage of the procedure) hyperspectral model and SEDm observations. This particular effect, which depends on the relative distribution of stellar and gaseous components in the host, has not been studied extensively for **HYPERGAL**, but we note it is efficient to disentangle host spectral features from SN spectrum even with sub-optimal input redshift and/or emission line fluxes. However, it effectively precludes the use of the residual host component for any *a posteriori* measurements, e.g. redshift or local measurement of  $H\alpha$  flux, yet crucial for local environment studies mentioned earlier (e.g. Rigault et al. 2020).

One could think of including a consistent redshift estimate directly in the **HYPERGAL** procedure, at the level of the hyperspectral model (to minimize artificial fluctuations of  $G(\lambda)$ ), but also at the level of the SN spectral typing (to reach a redshift consensus between the host and the SN). This would imply to include the intensive SED fit and/or the SN typing procedure in the



# Typing efficiency

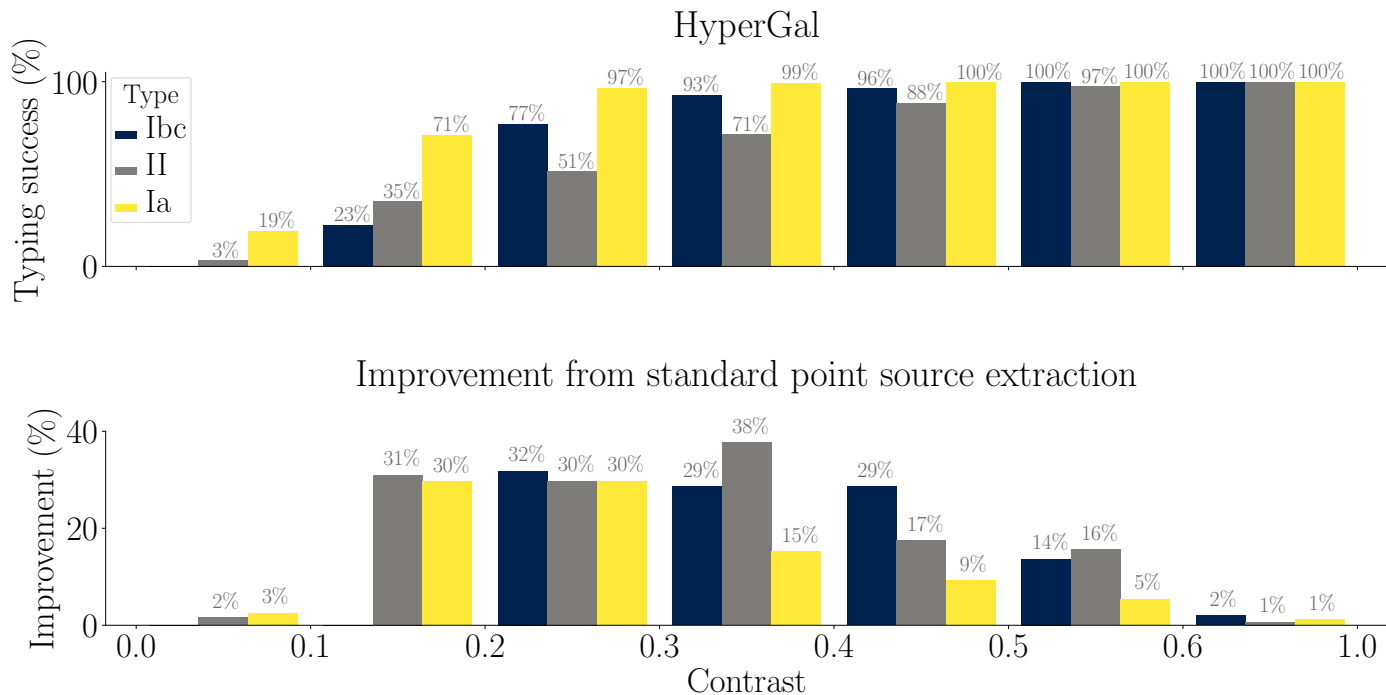


**Fig. 16.** Typing efficiency on the validation simulations. *Top panel:* rate of successful classification with **HYPERGAL** for each type of SN at different contrast levels. Results for  $c > 0.6$  are aggregated as the results vary very little. *Bottom panel:* improvement in typing compared to the standard extraction method.

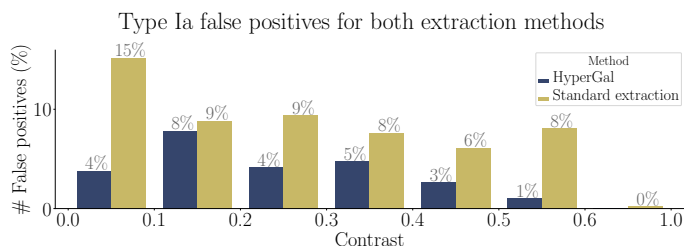


**Fig. 17.** False-Positive Rate in SN Ia classification for both extraction methods as a function of contrast.

minimization loop, computationally costly in either cases. Another major **HYPERGAL** development would be to use the SEDm cube, a rich and faithful observation of the host galaxy at the position of the transient, as additional hyperspectral constraints in the SED fitting process. Both developments would push the concept of an SED fitter merely used as a spectral interpolator to its limit. It would then probably be preferable to switch to other more efficient methods such as physics-enabled deep learning (Boone 2021).

## 5. Conclusion

This paper presents **HYPERGAL**, a fully automated scene modeler for the transient typing with the SEDm (Blagorodnova et al. 2018). The core of this pipeline is based on the use of archival photometric observations of the host galaxy, taken before the SN explosion. Knowing the physical processes in place within galaxies, as encoded in the SED fitter **CIGALE**, the spectral properties of the host are modeled, adjusted, and scaled appropriately to create a hyperspectral model of the host galaxy. This 3D in-

trinsic model is then convolved with the spectro-spatial instrumental responses of the SEDm, and projected in the space of the observations. A full scene model, including the structured host galaxy, the point source transient and a smooth background, is finally produced to match the SEDm observations, allowing the extraction of the SN spectrum from a highly contaminated environment.

The pipeline is validated on a large set of realistic simulated SEDm observations, covering a wide variety of observation conditions (airmass, seeing and PSF parameters), scene details (host morphology, distance to the host, host/SN contrast) and transient types. The contrast distribution is estimated from about 3000 observed SNe Ia of the ZTF Cosmology SN Ia DR2 paper to come (Rigault et al. in prep). The transient spectra in the 5000 simulations are then extracted with **HYPERGAL** and compared to the historical point-source method, which ignores the structured host component.

The most important results concern **HYPERGAL** efficiency in spectroscopically typing SNe, a key objective of the SEDm instrument. The full scene modeler shows an ability to correctly classify  $\sim 95\%$  of the observed SNe Ia under a realistic contrast distribution. For a contrast  $c \geq 0.2$  (more than 90% of the observations), nearly 99% of the SNe Ia are correctly classified. Compared to the standard extraction method, **HYPERGAL** correctly classifies nearly 20% more SNe Ia between  $0.1 < c < 0.6$ , representing  $\sim 50\%$  of the observation conditions.

The false positive rate for **HYPERGAL** is less than 5% for contrasts between 0.1 and 0.6, and less than 2% for  $c > 0.1$  ( $> 99\%$  of the observations); this is half as much as the standard extraction method.

**HYPERGAL** has demonstrated its ability to extract and classify the spectrum of an SN even in the presence of strong contami-

nation from its host galaxy. The improvement compared to the standard method is significant: this will noticeably improve the statistic of the SNe Ia sample for the ZTF survey while reducing a potential environmental bias, and will ultimately impact the precision of the cosmological analyses.

*Acknowledgements.* This project has received funding from the Project IDEX-LYON at the University of Lyon under the Investments for the Future Program (ANR-16-IDEX-0005), and from the European Research Council (ERC) under the European Union’s Horizon 2020 research and innovation programme (grant agreement n°759194 - USNAC). The SED Machine is based upon work supported by the National Science Foundation under Grant No. 1106171. Based on observations obtained with the Samuel Oschin Telescope 48-inch and the 60-inch Telescope at the Palomar Observatory as part of the Zwicky Transient Facility project. ZTF is supported by the National Science Foundation under Grant No. AST-1440341 and a collaboration including Caltech, IPAC, the Weizmann Institute for Science, the Oskar Klein Center at Stockholm University, the University of Maryland, the University of Washington, Deutsches Elektronen-Synchrotron and Humboldt University, Los Alamos National Laboratories, the TANGO Consortium of Taiwan, the University of Wisconsin at Milwaukee, and Lawrence Berkeley National Laboratories. Operations are conducted by COO, IPAC, and UW. This research made use of `PYTHON` (Van Rossum & Drake 2009), `ASTROPY` (Astropy Collaboration et al. 2013, 2018), `MATPLOTLIB` (Hunter 2007), `NUMPY` (van der Walt et al. 2011; Harris et al. 2020), `SCIPY` (Jones et al. 2001; Virtanen et al. 2020). We thank their developers for maintaining them and making them freely available.

## References

- Astropy Collaboration, Price-Whelan, A. M., Sipőcz, B. M., et al. 2018, *AJ*, 156, 123
- Astropy Collaboration, Robitaille, T. P., Tollerud, E. J., et al. 2013, *A&A*, 558, A33
- Barbary, K. 2016, *Journal of Open Source Software*, 1, 58
- Battisti, A. J., Calzetti, D., & Chary, R. R. 2016, *ApJ*, 818, 13
- Bellm, E. C., Kulkarni, S. R., Graham, M. J., et al. 2019, *PASP*, 131, 018002
- Bertin, E. & Arnouts, S. 1996, *A&AS*, 117, 393
- Betoule, M., Kessler, R., Guy, J., et al. 2014, *A&A*, 568, A22
- Blagorodnova, N., Neill, J. D., Walters, R., et al. 2018, *PASP*, 130, 035003
- Blondin, S. & Tonry, J. L. 2007, *ApJ*, 666, 1024
- Bolton, A. S., Schlegel, D. J., Aubourg, É., et al. 2012, *AJ*, 144, 144
- Boone, K. 2021, *AJ*, 162, 275
- Boquien, M., Burgarella, D., Roehlly, Y., et al. 2019, *A&A*, 622, A103
- Briday, M., Rigault, M., Graziani, R., et al. 2022, *A&A*, 657, A22
- Bruzual, G. & Charlot, S. 2003, *MNRAS*, 344, 1000
- Buat, V., Boquien, M., Malek, K., et al. 2018, *A&A*, 619, A135
- Burgarella, D., Buat, V., & Iglesias-Páramo, J. 2005, *MNRAS*, 360, 1413
- Buton, C., Copin, Y., Aldering, G., et al. 2013, *A&A*, 549, A8
- Chabrier, G. 2003, *PASP*, 115, 763
- Chambers, K. C., Magnier, E. A., Metcalfe, N., et al. 2016, arXiv e-prints, arXiv:1612.05560
- Charlot, S. & Fall, S. M. 2000, *ApJ*, 539, 718
- Chevallard, J., Curtis-Lake, E., Charlot, S., et al. 2019, *MNRAS*, 483, 2621
- Childress, M., Aldering, G., Antilogus, P., et al. 2013, *ApJ*, 770, 107
- da Cunha, E., Charlot, S., & Elbaz, D. 2008, *MNRAS*, 388, 1595
- Dale, D. A., Helou, G., Magdis, G. E., et al. 2014, *ApJ*, 784, 83
- Dask Development Team. 2016, *Dask: Library for dynamic task scheduling*
- Dembinski, H., Ongmongkolkul, P., Deil, C., et al. 2020
- DESI Collaboration, Aghamousa, A., Aguilar, J., et al. 2016, arXiv e-prints, arXiv:1611.00036
- Dhawan, S., Goobar, A., Smith, M., et al. 2022, *MNRAS*, 510, 2228
- Drake, A. J., Djorgovski, S. G., Mahabal, A., et al. 2009, *ApJ*, 696, 870
- Fremling, C., Miller, A. A., Sharma, Y., et al. 2020, *ApJ*, 895, 32
- Gillies, S. et al. 2007–, *Shapely: manipulation and analysis of geometric objects*
- Graham, M. J., Kulkarni, S. R., Bellm, E. C., et al. 2019, *PASP*, 131, 078001
- Guy, J., Astier, P., Baumont, S., et al. 2007, *A&A*, 466, 11
- Guy, J., Astier, P., Nobili, S., Regnault, N., & Pain, R. 2005, *A&A*, 443, 781
- Harris, C. R., Millman, K. J., van der Walt, S. J., et al. 2020, *Nature*, 585, 357
- Hunter, J. D. 2007, *Computing in Science & Engineering*, 9, 90
- Inoue, A. K. 2011, *MNRAS*, 415, 2920
- James, F. & Roos, M. 1975, *Computer Physics Communications*, 10, 343
- Jones, D. O., Scolnic, D. M., Riess, A. G., et al. 2017, *ApJ*, 843, 6
- Jones, E., Oliphant, T., & Peterson, P. 2001, *SciPy: Open Source Scientific Tools for Python*
- Jordahl, K. 2014, *GeoPandas: Python tools for geographic data*
- Kaiser, N., Aussel, H., Burke, B. E., et al. 2002, in *Society of Photo-Optical Instrumentation Engineers (SPIE) Conference Series*, Vol. 4836, *Survey and Other Telescope Technologies and Discoveries*, ed. J. A. Tyson & S. Wolff, 154–164
- Kelly, P. L., Hicken, M., Burke, D. L., Mandel, K. S., & Kirshner, R. P. 2010, *ApJ*, 715, 743
- Kim, Y. L., Rigault, M., Neill, J. D., et al. 2022, *PASP*, 134, 024505
- Law, N. M., Kulkarni, S. R., Dekany, R. G., et al. 2009, *PASP*, 121, 1395
- Malek, K., Buat, V., Roehlly, Y., et al. 2018, *A&A*, 620, A50
- Noll, S., Burgarella, D., Giovannoli, E., et al. 2009, *A&A*, 507, 1793
- Pruzhinskaya, M. V., Novinskaya, A. K., Pauna, N., & Rosnet, P. 2020, *MNRAS*, 499, 5121
- Rigault, M., Aldering, G., Kowalski, M., et al. 2015, *ApJ*, 802, 20
- Rigault, M., Brinnet, V., Aldering, G., et al. 2020, *A&A*, 644, A176
- Rigault, M., Copin, Y., Aldering, G., et al. 2013, *A&A*, 560, A66
- Rigault, M., Neill, J. D., Blagorodnova, N., et al. 2019, *A&A*, 627, A115
- Rigault, M., Smith, M., et al. in prep
- Rubin, D., Aldering, G., Antilogus, P., et al. 2022, arXiv e-prints, arXiv:2205.01116
- Shappee, B. J., Prieto, J. L., Grupe, D., et al. 2014, *ApJ*, 788, 48
- Stone, J. & Zimmerman, J. 2001, *Index of Refraction of Air*
- Sullivan, M., Conley, A., Howell, D. A., et al. 2010, *MNRAS*, 406, 782
- Tonry, J. L., Denneau, L., Heinze, A. N., et al. 2018, *PASP*, 130, 064505
- Tonry, J. L., Stubbs, C. W., Lykke, K. R., et al. 2012, *ApJ*, 750, 99
- van der Walt, S., Colbert, S. C., & Varoquaux, G. 2011, *Computing in Science & Engineering*, 13, 22
- Van Rossum, G. & Drake, F. L. 2009, *Python 3 Reference Manual* (Scotts Valley, CA: CreateSpace)
- Virtanen, P., Gommers, R., Oliphant, T. E., et al. 2020, *Nature Methods*, 17, 261
- Waters, C. Z., Magnier, E. A., Price, P. A., et al. 2020, *ApJS*, 251, 4